nature communications

Article | Article in Press

https://doi.org/10.1038/s41467-026-79472-y

# Interfacial mechanisms of gas-bubble friction

Received: 13 February 2026

Accepted: 15 October 2026

Published online: 19 November 2026

Check for updates

Shishuang Zhang[1,2,7], Huadong Tian[1,2,7], Jiajun Li[1,2], Zhikao Li[3], Jingyi Wang[4], Wei Sun[1], Hans-Jürgen Butt[5], Lei Xie[1,2,8] ✉ & Hongbo Zeng[6,8] ✉

Friction at solid-liquid interfaces is typically interpreted through classical contact mechanics, but molecular origins of gas-bubble friction in aqueous environments remain elusive. Here we report the direct quantification of gas-bubble friction at solid surfaces using atomic force microscopy with nano-newton resolution. We show that bubbles enter a contact-line friction regime only after film-mediated attachment, with static and kinetic responses that reflect contact-line pinning and sliding. On octadecyltrichlorosilane-grafted substrates, friction varies non-monotonically with surface hydrophobicity, peaking at intermediate hydrophobicity due to enhanced chemical heterogeneity. Surface chemistry and nanostructure further regulate energy dissipation, with relatively low friction on uniformly rough polydimethylsiloxane-grafted surfaces. Oxygen bubbles generate higher friction than air, nitrogen and carbon dioxide bubbles, as supported by molecular dynamics simulations that implicate gas-specific intermolecular interactions in contact-line dissipation. These findings provide molecular-level insight into gas-bubble friction, with implications for friction-tunable interfaces in catalysis, microfluidics, and medical applications.

Friction is a universal yet intricate phenomenon in nature, governing how energy is dissipated whenever two surfaces move relative to one another[1,2]. While the fundamentals of solid-solid friction have been extensively studied for their central role in mechanical, tribological, and engineering systems[3,4], our understanding of friction at soft and deformable interfaces remains incomplete. Recent advances have revealed that water droplets sliding on solid surfaces exhibit frictional behavior analogous to classical solids, characterized by distinct static (depinning) and kinetic regimes, which underpins advances in nanotechnology, microfluidics, and drag-reducing materials[5,6]. In contrast, the frictional dynamics of gas bubbles, particularly microbubbles at solid/water interfaces, remain virtually underexplored. This knowledge gap is particularly relevant to electrolysis, flotation, catalysis, power generation, adhesion switching, and many other fields, where efficient sliding and detachment of microbubbles are essential for sustaining mass transport and interfacial activity[7–10]. In many of these systems, bubble accumulation and contact-line pinning compromise transport efficiency by blocking active sites, increasing hydrodynamic resistance, and suppressing interfacial renewal[11,12]. Therefore, understanding and controlling bubble-solid friction is essential for rationally engineering bubble mobility, residence time, and detachment dynamics across multiphase technologies. Despite their ubiquity, the fundamental mechanism dictating bubble-solid

[1]School of Minerals Processing and Bioengineering, Central South University, Changsha, P. R. China. [2]Future Resources Interface Science and Intelligent Application Research Center (FRISIARC), Changsha, P. R. China. [3]Department of Chemical and Biological Engineering, Monash University, Clayton, VIC, Australia. [4]College of Chemistry and Chemical Engineering, Southwest Petroleum University, Chengdu, P.R. China. [5]Max Planck Institute for Polymer Research, ., Mainz, Germany. [6]Department of Chemical and Materials Engineering, University of Alberta, Edmonton, AB, Canada. [7]These authors contributed equally: Shishuang Zhang, Huadong Tian. [8]These authors jointly supervised this work: Lei Xie, Hongbo Zeng. ✉e-mail: lei.xie@csu.edu.cn; hongbo.zeng@ualberta.ca

friction and energy dissipation has received less quantitative investigation.

The sliding of rigid bodies, droplets, or bubbles on an inclined solid surface occurs only when the driving force exceeds resistance, followed by acceleration to steady state[13,14]. Analogous to solid or droplet friction, a sliding bubble is expected to transition from a static, depinning-dominated regime to a kinetic regime with constant friction. This naturally raises a fundamental question: How does friction evolve during bubble sliding? In rigid or viscous systems, molecules within the contact zone remain relatively immobile, and intermolecular interactions can contribute to frictional energy loss[15–17]. For bubbles, in contrast, gas molecules adjacent to solid surface undergo rapid thermal motion and continuous exchange with the bulk gas on timescales far shorter than sliding motion[18,19]. Such a dynamic and transient gas-solid interface challenges conventional frictional paradigms and raises a central question: how does contact-line dissipation govern bubble friction, and to what extent do gas-solid interactions modulate interfacial energy loss?

To date, bubble friction has only been inferred indirectly from advancing and receding contact angles via the Kawasaki-Furmidge relation[20–22]. However, for microbubbles, accurately determining the friction force by tracking dynamic contact angles and contact widths is challenging due to their micron-scale dimensions and limited optical resolution[23,24]. Consequently, the evolution of friction force and its dependence on sliding velocity remain not fully understood. Although recent capillary-based methods have enabled micronewton-scale measurements of droplet friction[25,26], these approaches are inadequate for micron-sized bubbles. The atomic force microscope (AFM) experimental setup offers a promising pathway to overcome these limitations. As a nanomechanical technique capable of measuring pico- to nanonewton forces, AFM has been widely used to quantify microbubble-surface interactions (e.g., van der Waals and hydrophobic interactions) in aqueous environments[27,28]. However, direct and quantitative measurement of bubble-solid friction has remained difficult to quantify experimentally. Here, we use bubble probe AFM to directly resolve the frictional evolution of microbubbles sliding on submerged solids with nanonewton sensitivity, revealing how film-mediated attachment establishes a contact-line friction regime and how bubble-specific processes regulate the resulting dissipation. We show that bubble friction occurs only after film-mediated contact line formation, is modulated by surface nanostructure and chemistry, and is further governed by gas-specific intermolecular interactions at the moving boundary.

In principle, bubble friction can be accessed via two different AFM configurations: (I) normal driving scheme: the cantilever is driven normally to slide a bubble attached to the vertical substrate downward, or (II) lateral driving scheme: a bubble attached to the cantilever is driven laterally to slide along a horizontal substrate. In Scheme I, the descending cantilever exerts a controlled normal thrust until the bubble depins and begins to slide, as illustrated in Fig. 1a, which allows the capture of entire frictional evolution from static to kinetic regimes. In this geometry, the cantilever mechanically constrains bubble displacement during sliding, effectively acting as a physical barrier that stabilizes the bubble throughout the measurement. In

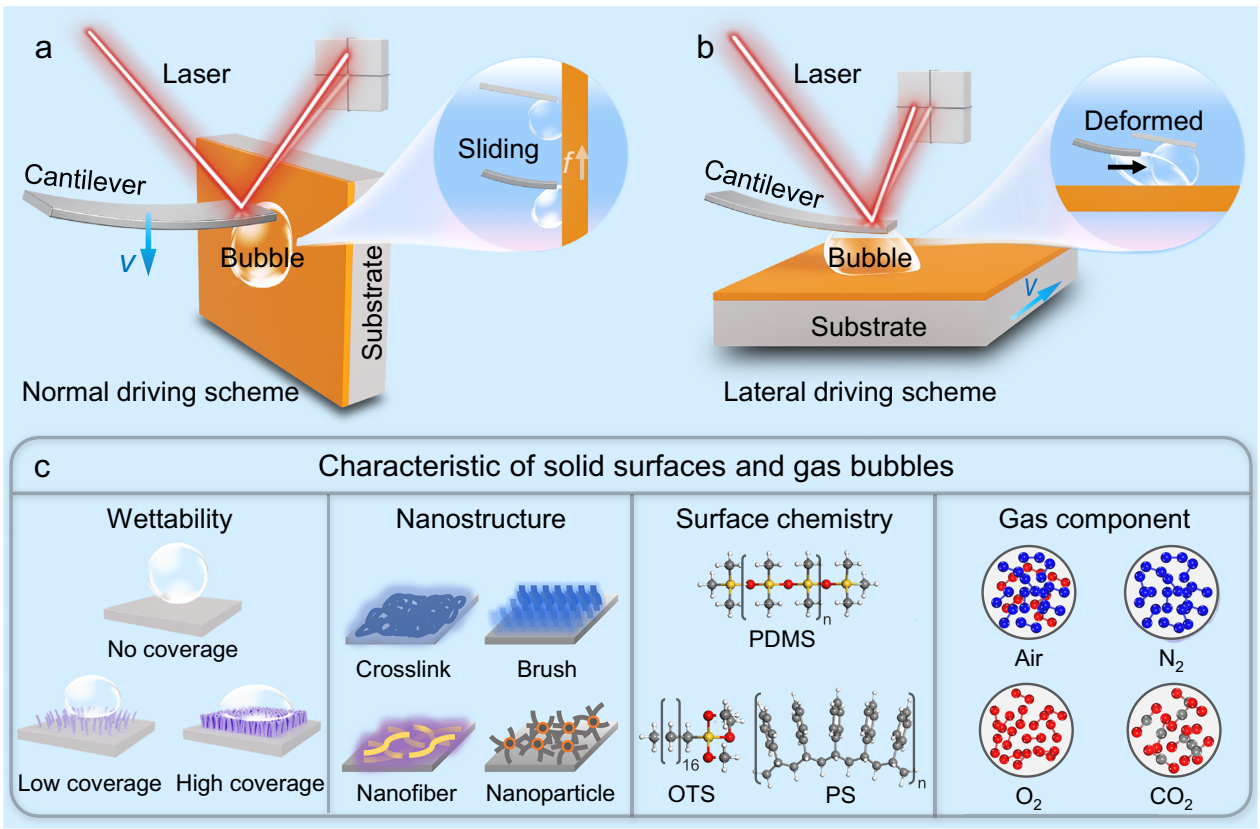



**Fig. 1 | Schematic of AFM-based bubble-solid friction measurements. a** Scheme I, in which the cantilever-mounted bubble probe is driven vertically downward to slide the bubble against the substrate. The enlarged view presents the bubble's downward sliding and the corresponding upward frictional force from a front-view perspective. *f* denotes friction force during bubble sliding. **b** Scheme II, in which the substrate is driven laterally relative to the cantilever-mounted bubble probe. The blue arrows indicate the driven component in each configuration. The enlarged view presents the bubble deformation from a side-view perspective. **c** Schematic illustration of surface characteristics (wettability, nanostructure, and chemistry) and gas composition investigated during friction measurements. AFM atomic force microscopy, PDMS polydimethylsiloxane, OTS octadecyltrichlorosilane, PS polystyrene. Atom colors: C, gray; H, white; O, red; Si, yellow; N, blue.

contrast, Scheme II (Fig. 1b) involves lateral translation of the substrate beneath a bubble attached to the cantilever. In this configuration, the cantilever cannot effectively confine bubble motion along the sliding direction, which is less suitable for hydrophobic surfaces. In this case, bubble attachment to the cantilever may be disrupted due to strong bubble-substrate adhesion, thereby inducing relative motion between bubble and cantilever instead. Therefore, Scheme I with wider applicability and more reliability is adopted to quantify bubble friction in this work. Using this approach, we systematically decipher how surface characteristics (e.g., wettability, nanostructure, and chemistry), gas composition, and sliding velocity modulate bubble-solid friction (Fig. 1c), further supported by molecular dynamics (MD) simulations that elucidate the molecular mechanisms of energy dissipation. These findings establish the quantitative framework for frictional dissipation of gas bubbles at the microscopic level, bridging a long-standing gap in our understanding of bubble friction and the related interfacial processes.

## Results

### Force evolution during bubble sliding

To unravel the molecular origins of bubble-solid friction, we examined silicon substrates with tuned surface hydrophobicity, achieved by varying the coverage of octadecyltrichlorosilane (OTS). The resulting smooth surfaces (Supplementary Figs. 1 and 2) exhibited static water contact angles of 90°, 45° and 0°, denoted as silicon-OTS-90, silicon-OTS-45 and silicon-OTS-0, respectively. These model surfaces enabled the quantitative investigation of how bubble-solid friction develops and how surface wettability influences the frictional energy dissipation.

For fully hydrophobic silicon-OTS-90 and partially hydrophobic silicon-OTS-45, bubble readily attached to the surfaces once the confined water film ruptured, forming a three-phase contact line. As AFM cantilever was driven downward, the deflection monotonically increased until critical thresholds of 220 ± 1 nN and 260 ± 3 nN were reached (Fig. 2a, b and Supplementary Table 1). Within the Kawasaki-Furmidge description, the force peak represented the maximum static friction, the resistance arising from the energy barrier associated with contact-line pinning. Once this threshold ($f_{th}$) was exceeded, bubble began to slide under the imposed constant driving velocity, and the measured force relaxed to a stable force plateau of 210 ± 1 nN and 243 ± 2 nN (Supplementary Table 1), representing the kinetic friction regime (corresponding to $f_{kin}$). Accordingly, the entire force-time profile could be classified into three distinct regimes: static, transition, and kinetic. The existence of a threshold force explains why buoyancy-driven bubbles only start sliding upward when the surface tilt reaches a critical angle[29,30], analogous to droplet-solid friction, where a threshold force must be overcome to initiate downhill motion. In contrast, on the fully hydrophilic silicon-OTS-0, a stable water film remained confined between bubble and solid surface, preventing their spontaneous attachment (Fig. 2f)[27,31,32]. As a result, the bubble had to be gently pre-pressed against the surface for friction measurement. In the absence of a true three-phase contact line, the measured friction force was very weak, about 10-15 nN, as shown in Fig. 2c. This observation is consistent with the important role of interfacial wetting and contact-line formation in controlling liquid/bubble-solid friction[32].

Interestingly, silicon-OTS-90 with greater surface hydrophobicity showed lower friction than silicon-OTS-45. This phenomenon can be rationalized using the classical Kawasaki-Furmidge relation, where the maximum static friction scales with the contact angle hysteresis along the three-phase contact line. Here, silicon-OTS-90 displays a reduced hysteresis compared to silicon-OTS-45 (from ~21° to ~14°, Supplementary Table 2), leading to weaker contact-line pinning and thus a lower friction threshold. Therefore, bubble friction is not simply governed by static wettability, but is intimately linked to contact angle hysteresis. Mechanistically, the densely packed and chemically homogeneous OTS monolayer on silicon-OTS-90 (Fig. 2d) reduces hysteresis and interfacial energy loss, while the incomplete OTS coverage and higher molecular heterogeneity on silicon-TOS-45 (Fig. 2e) enhances contact-line anchoring and frictional dissipation[33].

For bubble friction measured via Scheme II, where the bubble attached to an AFM cantilever was driven laterally across the substrate, stable testing was only achieved on the hydrophilic surface (Supplementary Fig. 3). On silicone-OTS-90 and silicone-OTS-45, the bubble adhered so strongly to the substrate that it detached from the hydrophobized gold patch on the cantilever. The lateral cantilever motion induced pronounced bubble deformation and capillary resistance, which progressively increased the cantilever lateral deflection and immobilized the bubble on the substrate. For silicon-OTS-0, the bubble readily overcame the friction and moved smoothly with a tiny and nearly constant cantilever lateral deflection of ~0.2 nm, consistent with the behavior observed under Scheme I. Note that the lateral deflection signal of the cantilever was used to characterize the evolution of bubble friction in Scheme II, which could be converted to force based on the lateral spring constant.

### Surface nanostructure- and chemistry-governed friction

To examine whether this frictional evolution is a general feature of bubble motion, we extended our investigation to a diverse set of functional surfaces differing in nanostructure (smooth, unevenly rough, or uniformly rough) and surface chemistry, with the morphology illustrated in Supplementary Figs. 4 and 5. All the surfaces were fabricated on silicon wafers, including crosslinked polydimethylsiloxane (PDMS), slippery PDMS brushes (brush PDMS), nanoparticles grafted with slippery PDMS brushes (brush PDMS-NP), polystyrene (PS) film, OTS-grafted cellulose nanofibers (OTS-CNF), and OTS-grafted nanoparticles (OTS-NP). The measured friction across these various surfaces was summarized in Supplementary Table 1. On most surfaces, the static friction force exceeded the kinetic friction force (Fig. 3a, d–f), confirming that the transition from static to kinetic regimes is a general feature of bubble sliding. In contrast, on both slippery brush PDMS and brush PDMS-NP surfaces (Fig. 3b, c), the bubble transitioned from the static to the kinetic regime without a discernible intermediate state, yielding $f_{kin} \approx f_{th}$. Taking into account the inherent flexibility of such slippery PDMS brushes[34,35], their rapid conformational response allows the interface to reorganize instantaneously during sliding, suppressing contact-line pinning and eliminating the conventional frictional threshold. Such threshold-free bubble transport is highly desirable for continuous gas-release systems, where minimizing depinning barriers can facilitate spontaneous bubble removal and reduce interfacial blockage.

The temporal evolution of friction forces for PDMS surfaces with distinct topographies illustrates how surface nanostructure modulates the energy landscape of bubble sliding (Fig. 3a–c). On crosslinked PDMS, the friction force increased until reaching a peak of 245 ± 2 nN, after which it relaxed to a stable kinetic regime of 231 ± 3 nN (Fig. 3a). The energy dissipated during the transition regime arises from dynamic rearrangement of three-phase contact line[36]. However, the mobile PDMS brushes minimized such dissipation and enabled threshold-free sliding (Fig. 3b, c). The uniformly rough brush PDMS-NP exhibited even lower friction than the smooth brush PDMS, with $f_{kin}$ = 61 ± 1 nN compared to 92 ± 1 nN, revealing that uniform nanostructuring can enhance surface slipperiness. This effect likely originates from the free PDMS molecules residing between the uniformly distributed nanoparticles (Supplementary Figs. 4c, 5c), which form a meniscus even thicker than nanoparticle layer and thus lubricate bubble sliding (Fig. 3g)[37,38]. In addition, these free molecules may migrate to water-air interface and reduce surface tension of bubble, further suppressing bubble friction. A similar trend emerged among OTS-grafted surfaces with controlled nanostructures (silicon-OTS-90 vs. OTS-NP), where friction decreased from 210 ± 1 nN on smooth

https://doi.org/10.1038/s41467-026-79472-y

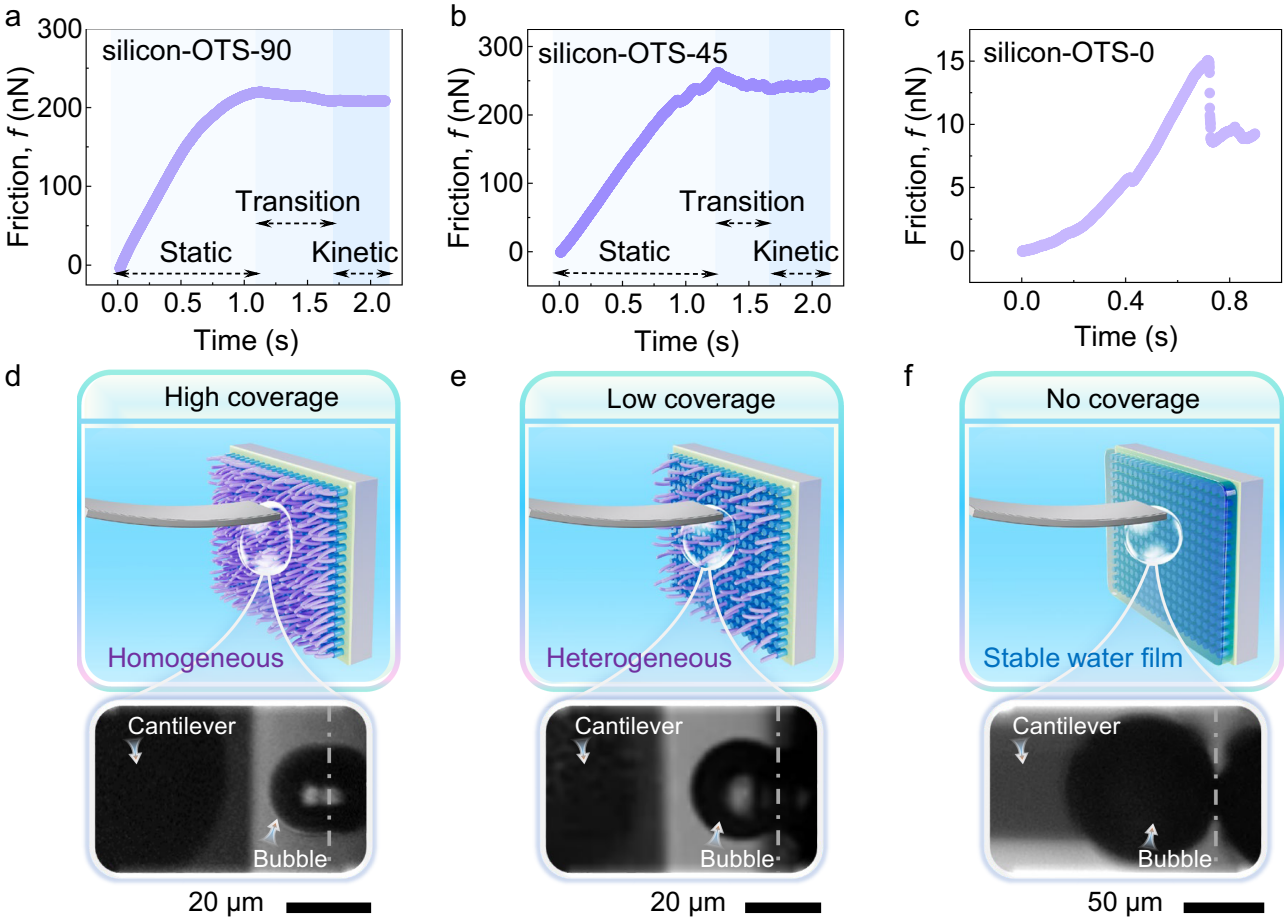



**Fig. 2 | Bubble friction on silicon substrates of various surface hydrophobicity.** Friction force curves for an air bubble (contact width $w \approx 20$ μm) sliding on **a** silicon-OTS-90, **b** silicon-OTS-45, and **c** silicon-OTS-0. Measurements were performed using Scheme I by vertically actuating the cantilever at a constant velocity of 5 μm $s^{-1}$. Schematic illustrations and corresponding representative bottom-view microscope images of bubble sliding on (**d**) silicon-OTS-90 (high OTS coverage), **e** silicon-OTS-45 (low OTS coverage), and the non-attached bubble state on (f), silicon-OTS-0 (no OTS coverage). It should be noted that each microscope image is divided by a gray dashed line: the cantilever and bubble are shown on the left, whereas their optical reflections appear on the right. Scale bars: 20 μm in **d** and **e**; 50 μm in (**f**). Silicon-OTS-90, silicon-OTS-45, and silicon-OTS-0 denote silicon substrates with water contact angles in air of approximately 90°, 45°, and 0°, respectively, obtained by varying the coverage of OTS. The static underwater air contact angles were ~90° and ~135° for silicon-OTS-90 and silicon-OTS-45, respectively, with corresponding advancing/receding angles of ~97°/83° and ~143°/122°. On silicon-OTS-0, the bubble did not spontaneously attach because a stable confined water film separated the bubble from the solid surface. Therefore, conventional advancing/receding underwater air contact angles could not be measured; this non-attached state represents the limiting wetting condition corresponding to an underwater air contact angle approaching 180° (Supplementary Table 2). Abbreviation: OTS, octadecyltrichlorosilane. The experiments shown in (**d**–**f**) were independently repeated three times with similar results. Source data are provided as a Source Data file.

silicon-OTS-90 to 173 ± 5 nN on uniformly rough OTS-NP (Figs. 2a, 3f). In contrast, the irregular topography of unevenly rough OTS-CNF induced the frequent pinning-depinning events, manifesting as discrete force spikes and the absence of a well-defined kinetic regime, leading to the highest bubble friction (270 ± 15 nN in Fig. 3e, g) among the three OTS surfaces. Such surfaces exhibiting stronger pinning and larger frictional resistance may be beneficial for applications requiring prolonged bubble retention or localization, such as flotation and gas-capture processes.

The comparisons between surfaces of similar topology but different chemistry further reveal how molecular flexibility governs bubble frictional dynamics. Although both brush PDMS and silicon-OTS-90 are smooth grafted surfaces, brush PDMS exhibited a direct static-to-kinetic transition and a friction level approximately 50% lower than that of silicon-OTS-90 with an intermediate transition (Figs. 2a, 3b). Similarly, for the uniformly rough grafted surfaces, friction force on brush PDMS-NP was ~113 nN lower than that on OTS-NP (Fig. 3c, f). These results indicate that bubbles slide more easily on PDMS-grafted surfaces than OTS-grafted surfaces, probably attributed to the low glass transition temperature and intrinsic segmental flexibility of Si-O-Si backbones, which enable molecular rearrangement and rapid stress relaxation (Fig. 3h)[34,35,39]. For PS film, the frictional response was comparable to that of crosslinked PDMS, yet with a higher force value of 247 ± 1 nN (Fig. 3a, d). Given that benzene ring is a part of PS backbone, its rigidity and polarity coupled with π-π stacking interactions could enhance the friction[40,41], relative to the flexible and non-polar methyl side chains of PDMS (Fig. 3h).

## Contact-line scaling and gas-specific bubble friction

To determine how bubble-surface friction scales with contact width, a series of friction force measurements were conducted on silicon-OTS-90 substrates by varying the bubble volume. The kinetic friction force $f_{kin}$ increased linearly with contact width $w$, and force data at different velocities collapsed into their $f_{kin}(w)$ master straight lines (Fig. 4a; see representative raw force data in Supplementary Fig. 6). The fitting equations and parameters for these data are summarized in Supplementary Table 3. In addition to contact-line dissipation, hydrodynamic drag arising from bulk fluid flow around the bubble may

https://doi.org/10.1038/s41467-026-79472-y

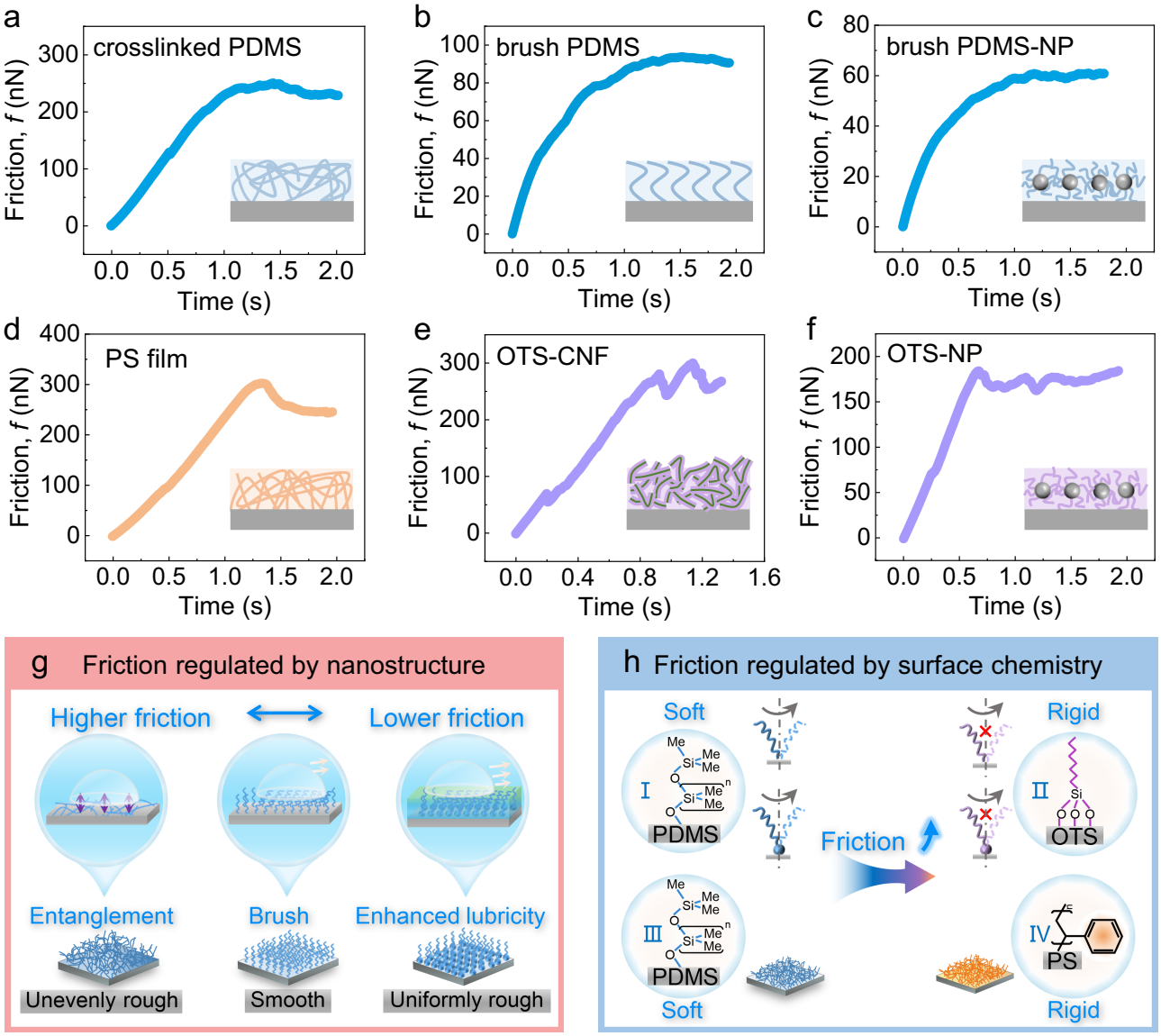



**Fig. 3 | Bubble friction on functional solid surfaces.** Friction force curves for air bubbles sliding on **a** crosslinked PDMS, **b** brush PDMS, **c** brush PDMS-NP, **d** PS film, **e** OTS-CNF, and **f** OTS-NP, respectively. Measurements were performed using Scheme I at a constant velocity of 5 μm $s^{-1}$. Before bubble motion, the gas-solid contact width $w$ was measured to be ~20 μm for each surface, with values of approximately 19.6, 18.9, 19.6, 20.7, 18.9, and 17.8 μm for panels **a**–**f**, respectively. **g** Schematic showing the effect of nanostructure on bubble friction. On the unevenly rough surface, irregular topography promotes frequent contact-line pinning and depinning, resulting in higher friction. In contrast, smooth surface reduces contact-line dissipation, while the uniformly rough surface further lowers friction primarily because free molecules between the nanoparticles form a thicker lubricating meniscus and enhance interfacial lubricity. **h** Schematic showing the effect of surface chemistry on bubble friction. Flexible PDMS chains can rapidly rearrange and respond to contact-line motion during bubble sliding, reducing contact-line pinning and friction, whereas the more rigid OTS and PS surfaces exhibit higher frictional resistance. The blue-to-purple arrow indicates increasing friction from softer to more rigid surface chemistries. The advancing/receding underwater air contact angles on crosslinked PDMS, brush PDMS, brush PDMS-NP, PS film, OTS-CNF, and OTS-NP surfaces were ~85°/68°, ~81°/74°, ~71°/69°, ~98°/80°, ~102°/82°, and ~94°/83°, respectively, as summarized in Supplementary Table 2. PDMS polydimethylsiloxane, PS polystyrene, OTS octadecyltrichlorosilane, CNF cellulose nanofiber, NP nanoparticle, Me methyl. Source data are provided as a Source Data file.

contribute to the measured friction. Considering the small bubble sizes and low sliding velocities used in this study, the hydrodynamic drag was estimated to be on the order of $10^{-2}$ nN using Supplementary Eq. (1) in Supplementary Note 1[42], which is several orders of magnitude lower than the measured friction forces (~$10^2$ nN), rendering its contribution to friction negligible. Thus, the linear correlation between $f_{kin}$ and $w$ indicates that energy dissipation is dominated by contact line friction, consistent with droplet friction models[43,44]. To further elucidate the empirical correlation of friction force and sliding velocity, the kinetic friction force was plotted in its normalized form $f_{kin}/2r$ ($w = 2r$) against velocity $U$. As shown in Fig. 4b (see representative raw force data in Supplementary Fig. 7, and fitting parameters in Supplementary Table 3), the normalized friction force $f_{kin}/2r$ exhibited a nonlinear increment with velocity $U$, indicating a velocity-dependent dynamic rearrangement at the three-phase contact line.

Given that air bubbles are primarily composed of nitrogen ($N_2$) and oxygen ($O_2$), an interesting question arises: How does the friction of air bubbles relate to that of their individual gas components? Considering the distinct chemical nature of carbon dioxide ($CO_2$) as an acidic gas, it is important to examine whether its friction force differs from that of neutral gases. To address these questions, single-component gases (e.g., $N_2$, $O_2$, and $CO_2$) were injected into their

https://doi.org/10.1038/s41467-026-79472-y

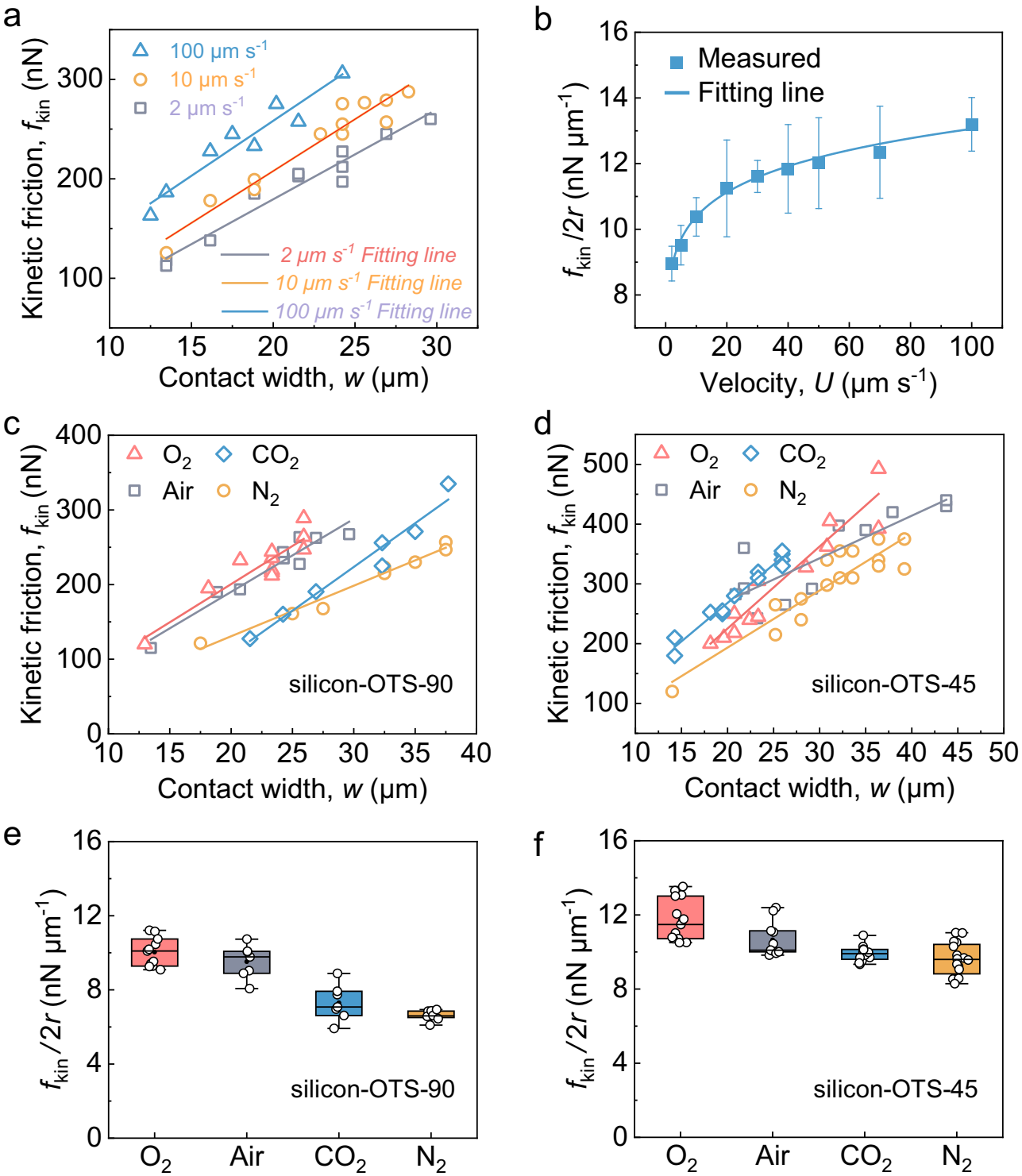



**Fig. 4 | Kinetic friction force dependence on contact width, velocity and gas component. a** Kinetic friction force as a function of contact width for air bubbles sliding on silicon-OTS-90 at three different velocities: 2 μm $s^{-1}$, 10 μm $s^{-1}$ and 100 μm $s^{-1}$. **b** Normalized kinetic friction forces, $f_{kin}/2r$ ($w = 2r$), plotted as a function of sliding velocity $U$, where $f_{kin}$ is the kinetic friction force, $w$ is the contact width, and $r$ is the bubble base radius. Kinetic friction force as a function of contact width for $O_2$, air, $CO_2$, and $N_2$ bubbles sliding at 5 μm $s^{-1}$ on (**c**) silicon-OTS-90 and **d** silicon-OTS-45, respectively. Corresponding normalized kinetic friction force, $f_{kin}/2r$ ($w = 2r$), for $O_2$, air, $CO_2$ and $N_2$ bubbles on (**e**) silicon-OTS-90 and **f** silicon-OTS-45, respectively. The fitting equations and parameters for these data are summarized in Supplementary Table 3. Data are presented as mean ± SD for panel b. For e and f, the center line indicates the median, the box bounds indicate the 25th and 75th percentiles, and the whiskers indicate the minimum and maximum values. For **a**, $n = 11$, 12 and 8 at 2, 10 and 100 μm $s^{-1}$, respectively; for **b**, $n = 11$, 9, 12, 13, 7, 17, 9, 9 and 8 at 2, 5, 10, 20, 30, 40, 50, 70 and 100 μm $s^{-1}$, respectively; for **c**, $n = 11$, 10, 9 and 10 for $O_2$, air, $CO_2$ and $N_2$, respectively; for **d**, $n = 13$, 12, 12, and 16, respectively; for **e**, $n = 11$, 7, 7, 8 for $O_2$, air, $CO_2$ and $N_2$, respectively; and for **f**, $n = 13$, 11, 12, 16 for $O_2$, air, $CO_2$ and $N_2$, respectively. Each n represents independent measurements using separately generated bubbles. OTS octadecyltrichlorosilane. Source data are provided as a Source Data file.

respective saturated solutions to generate microbubbles for friction measurements on silicon-OTS-90 and silicon-OTS-45 surfaces. On both surfaces, the friction force curves for $N_2$, $O_2$, and $CO_2$ bubbles followed the profiles identical to air bubbles, and the linear correlation between kinetic friction force and contact width remained applicable for these single-component bubbles (Fig. 4c, d; see representative raw force data in Supplementary Figs. 8, 9). The normalized kinetic friction forces were measured as 10.0, 9.5, 7.3, and 6.6 nN μm$^{-1}$ for $O_2$, air, $CO_2$ and $N_2$ bubbles on silicon-OTS-90, respectively (Fig. 4e), and 11.7, 10.7, 9.9, and 9.6 nN μm$^{-1}$ on silicon-OTS-45 (Fig. 4f). These results indicate that friction consistently followed the trend $O_2$ > air > $CO_2$ > $N_2$ on both surfaces. The emergence of gas-specific friction demonstrates that bubble transport is not solely controlled by surface properties, but can also depend intrinsically on gas composition. This behavior introduces the possibility of selectively regulating bubble mobility and detachment according to gas type in multiphase systems. Bubble friction on silicon-OTS-90 was lower than that on silicon-OTS-45 for each gas composition, consistent with the trend observed for air bubbles (representative force curves shown in Supplementary Figs. 10, 11).

## Mechanisms of contact-line bubble friction

On the self-assembled OTS monolayer, the possible role of elastocapillary deformation governed by gas-water interfacial tension was considered as a possible origin of observed differences in single-gas bubble friction[21,45]. When a gas bubble rests on a solid substrate immersed in liquid, the vertical component of liquid-gas interfacial tension ($\gamma_l \sin\theta$) induces a localized deformation of the substrate, forming a wetting ridge at the three-phase contact line (Supplementary Fig. 12). Based on Supplementary Eqs. (2–4) in Supplementary Note 2, the height of wetting ridge can be ultimately estimated by $h \approx \frac{\gamma_L \sin\theta}{2\pi G} \ln\left(\frac{L}{\ell}\right)$[. Using the relevant material properties and geometric parameters, the characteristic ridge height falls within the range of ~0.27–0.38 nm for silicon-OTS surfaces with different wettabilities, which is non-negligible compared with the ~2.5 nm OTS monolayer[46]. During sliding, the motion of contact line dynamically deforms this ridge, leading to energy dissipation and thereby contributing to frictional resistance[22]. However, the measured friction trend among gases, $O_2$ > air > $CO_2$ > $N_2$, is not consistent with the reported water-gas interfacial tensions ($O_2$: 72.0 mN m$^{-1}$, air: 72.0 mN m$^{-1}$, $CO_2$: 65.0 mN m$^{-1}$, $N_2$: 72.0 mN m$^{-1}$)[28,47–49], indicating that the gas-specific friction cannot be accounted for by elastocapillary deformation.

Instead, intermolecular interactions between gas molecules and the alkyl-terminated OTS layer at the contact line, expected to remain within a physisorption regime[50–52], may contribute to gas-specific frictional behavior. First, these interactions regulate the gas adsorption dynamics and thus contact-line dissipation (Fig. 5a). As a bubble slides over solid surface, the three-phase boundary continuously interconvert between solid-water and solid-gas interfaces[53,54]. This process requires interfacial water to be displaced and restored, while gas molecules transiently enrich at the newly exposed hydrophobic surface before exchanging with the surrounding phase[55]. The resulting perturbation of local adsorption equilibrium provides additional molecular pathway for contact-line dissipation, with the gas identity governing the strength and timescale of the exchange. Note that these physical adsorption processes arise from non-bonded intermolecular interactions at the moving contact line[50,51]. Each cycle induces localized interfacial deformation and molecular-level energy dissipation, giving rise to gas-specific friction stemming from the differences in adsorption strength and residence time[52,56].

Moreover, gas-solid interactions can drive the subtle surface adaptation (Fig. 5b). According to adaptation theory, immersing a solid surface in water allows its interfacial molecular structure to reorganize in response to the surrounding environment[5]. Different gas-substrate interactions can affect the interfacial structure to varying degrees, which alters surface polarity, molecular ordering, or interfacial hydration. These gas-dependent interfacial modifications influence how the moving contact line interacts with the surface, further contributing to distinct frictional responses. Therefore, the intermolecular interaction-mediated contact-line dissipation and surface adaptation provide a coherent molecular framework for understanding gas-specific friction and associated contact angle hysteresis.

MD simulations were performed to elucidate how gas-solid interactions regulate adsorption dynamics and contact-line motion on OTS-grafted surfaces (Supplementary Figs. 13–16, and Supplementary Movies 1–8). The simulated sliding velocities of $O_2$, air, $CO_2$, and $N_2$ bubbles increased sequentially (Supplementary Table 4), revealing the descending order of friction forces, consistent with the above experimental results. For $O_2$, air, and $N_2$ bubbles, the extent of local contact-line deformation on both silicon-OTS-90 and silicon-OTS-45 (Fig. 5c, d) also followed the same trend, suggesting that gas-specific friction originates from differences in intermolecular interactions and their adsorption strength within the physisorption regime at the moving three-phase boundary.

To further quantify the adsorption behavior of gas bubbles, adsorption energies, mean molecular positions, and near-surface residence times were analyzed. The calculated adsorption energies followed the order $O_2$ > air> $CO_2$ > $N_2$ (Supplementary Fig. 17). Consistent with this trend, the mean molecular z-coordinate decreased from 38.48 Å for $N_2$ to 37.61 Å for $O_2$, indicating progressively closer proximity of gas molecules to the substrate (Supplementary Tables 5 and 6). The near-surface residence time increased in the same sequence, from 67.67 ps for $N_2$ to 87.77 ps for $O_2$ (Supplementary Table 6). All these results indicate that stronger gas-sold interactions retain gas molecules closer to the substrate and prolong their residence within the interfacial region, thereby slowing interfacial exchange at the moving contact line. This process increases molecular-scale energy dissipation and enhances contact-line friction. $O_2$ therefore exhibits the highest friction owing to its strongest interfacial affinity and longest residence behavior, whereas $N_2$ displays the weakest interfacial retention and correspondingly the lowest friction. Air, as a mixture of $O_2$ and $N_2$, shows an intermediate response. Interestingly, although the adsorption energy of $CO_2$ exceeds that of $N_2$, its residence time remains substantially lower than those of $O_2$ and air. This behavior may be associated with the distinct interfacial exchange dynamics of $CO_2$ arising from its partial dissolution and hydration in water[49], which facilitates gas-water exchange and reduces molecular retention at the moving interface.

## Bubble versus droplet friction

Droplet friction offers the most relevant reference for understanding bubble friction, as both involve energy dissipation associated with a moving three-phase contact line[5]. The two systems nevertheless differ in how the contact line is established and how viscous losses are distributed. For a sessile droplet deposited in air, the three-phase contact line is generally present from the outset. In contrast, a bubble approaches a submerged solid through an intervening water film, such that friction emerges only after a film-mediated entry process: the confined liquid film must drain, deform, and rupture before a stable contact line can form[57]. In the present geometry, this film-mediated attachment is therefore an entry condition for contact-line dissipation rather than a contribution to the post-attachment friction force itself.

After attachment, bubble friction enters a contact-line dissipation regime associated with contact-line motion. Once a three-phase contact line is established, bubble motion begins only when the driving force exceeds a depinning threshold, analogous to droplets. This static-to-kinetic transition and contact-line motion is governed by surface heterogeneity, roughness, and molecular mobility, consistent

https://doi.org/10.1038/s41467-026-79472-y

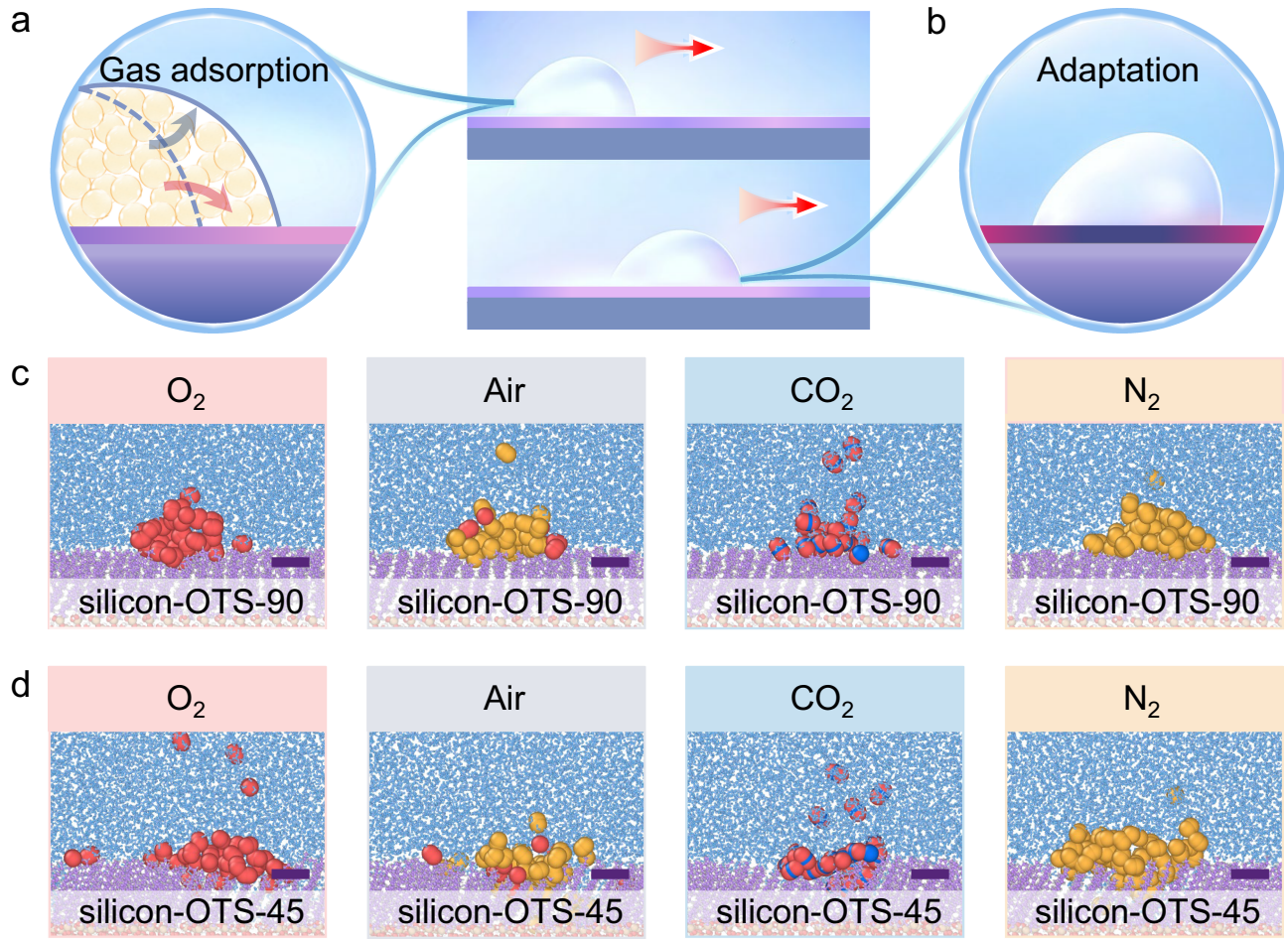



**Fig. 5 | Contact-line friction mediated by gas adsorption and surface adaptation arising from gas-solid intermolecular interaction. a** Schematic of local contact-line deformation at the advancing front and receding rear of a sliding bubble during an adsorption-desorption cycle. Pale orange spheres represent gas molecules. **b** Schematic of surface adaptation and associated changes in interfacial properties during bubble sliding. Representative snapshots of MD simulations showing the contact-line configurations of oxygen ($O_2$), air, carbon dioxide ($CO_2$), and nitrogen ($N_2$) bubbles sliding on **c** silicon-OTS-90 and **d** silicon-OTS-45 under a constant external driving force. Scale bars: 10 Å in (**c** and **d**). OTS octadecyltrichlorosilane. Red, orange, and blue represent O, N, and C atoms, respectively.

with the droplet-like force evolution[43]. Unlike droplets, however, the gas phase introduces additional molecular contributions at the moving boundary. Gas molecules near the contact line can transiently interact with solid surface and exchange with the surrounding gas or liquid phase as the boundary advances. As a result, contact-line friction in bubble systems is influenced not only by solid surface but also by the specific gas-solid intermolecular interactions. The experimental and simulation results are consistent with these near-surface interactions modulating contact-line mobility, although the present measurements do not uniquely separate this molecular contribution from all other contact-line losses.

The replacement of the liquid droplet by a gas bubble also changes the distribution of viscous dissipation. In droplet friction, viscous loss may occur within the liquid body and near the moving contact line region[14]. For an underwater bubble, internal gas-phase dissipation is negligible and the bulk-fluid contribution is mainly in the surrounding liquid[58]. Under the present low-speed aqueous conditions, an order-of-magnitude Stokes-drag estimate is much smaller than the measured forces. Because that estimate neglects wall confinement and deformation, it is used only to show that bulk drag is unlikely to dominate; hydrodynamic effects may become more important for larger bubbles, more viscous liquids, or higher velocities.

Surface adaptation may also contribute, because the moving contact line repeatedly switches the local surface environment between water-contacting and gas-contacting states[5]. Gas-dependent changes in interfacial structure could therefore alter contact-line mobility and reinforce the gas-specific contact-line friction. Additional interfacial response can further modulate bubble friction. Liquid-gas interfacial tension may deform the substrate near the contact line, analogous to elastocapillary deformation in droplet systems[45]. These effects may modulate the mobility of moving boundary, but do not supersede the dominant role of contact-line dissipation.

Therefore, bubble friction and droplet friction share a common contact-line framework after stable attachment, but they differ in how this framework is accessed and regulated. Bubble friction is preceded by thin film drainage and rupture, regulated at the contact line by gas-specific interfacial interactions, and accompanied by viscous dissipation shifted away from the gas phase into the surrounding liquid. These differences explain why bubbles show static and kinetic regimes reminiscent of droplets while also displaying frictional responses that are specific to gas bubbles at submerged solid surfaces, as summarized in Table 1.

## Discussion

Using AFM, we directly quantified the frictional evolution of gas-bubble sliding along submerged solid surfaces with nanonewton

**Table 1 | Comparison of major dissipation pathways in droplet and bubble friction**

| Mechanism | Droplet | Bubble | Comparison |
|---|---|---|---|
| Thin-film drainage and rupture | Pre-established three-phase contact line | Pre-attachment water-film drainage and rupture | Bubble-specific entry step |
| Static contact-line depinning | Pinning by roughness, heterogeneity and hysteresis | Pinning after three-phase contact-line formation | Shared after attachment |
| Kinetic contact-line friction | Contact-line motion over defects/ heterogeneity | Contact-line motion modulated by gas adsorption | Shared, with gas-specific modulation |
| Viscous/ hydrodynamic dissipation | Dissipation within droplet and near contact line | Dissipation in surrounding liquid | Redistributed in bubbles |
| Elastocapillary deformation | Wetting ridge on soft/adaptive substrates | Wetting ridge on soft/adaptive substrates | Shared, substrate-dependent |
| Surface adaptation | Interfacial reorganization | Interfacial reorganization modulated by gas adsorption | Shared, with gas-specific modulation |

resolution. The measurements show that bubbles enter a contact-line friction regime only after film-mediated attachment, which is a step absent in droplet motion. By systematically tuning surface wettability, nanoscale structure, and surface chemistry, we demonstrated how interfacial molecular organization dictates energy dissipation during bubble sliding. Notably, $O_2$ bubbles exhibited the highest friction among all gases examined, followed by air, $CO_2$ and $N_2$, a hierarchy that was further supported by MD simulations. This gas specificity indicates that gas-solid intermolecular interactions modulate contact-line dissipation through adsorption-desorption and interfacial exchange near the moving boundary, and surface adaptation may further tune contact-line mobility by altering the local interfacial state during bubble sliding. These results establish bubble friction as a contact line-dominated interfacial behavior that is accessed through film-mediated attachment, modulated by gas-specific interactions at the moving boundary, and accompanied by viscous dissipation mainly shifted into the surrounding liquid. These findings on molecularly engineered surfaces provide a molecular understanding of gas-solid friction and establish design principles for adaptive, drag-reducing, and friction-tunable interfaces, with relevance to multiphase processes and technologies such as electrolysis, flotation, catalysis, power generation, adhesion switching, microfluidics, soft robotics, and biomedical applications.

## Methods

### Preparation of solid surfaces

#### Reagents and materials

The reagents used for the preparation of solid surfaces included octadecyl trichlorosilane (OTS, 95%, Sigma-Aldrich), dichlorodimethylsilane (DCDMS, 99.5%, Sigma-Aldrich), poly(-diallyldimethylammonium chloride) (PDAC, 20 wt% in $H_2O$, Sigma-Aldrich), poly (4-styrene sulfonic acid) solution (PSS, 30 wt% in $H_2O$, Sigma-Aldrich), Sylgard 184 PDMS precursor (Dow Corning), Sylgard 184 curing agent (Dow Corning), toluene (99.5%, Sinopharm), ethanol (absolute, 99.5%, Sinopharm), hexane (98%, Sinopharm) and sodium chloride (NaCl, 99%, Sigma-Aldrich). OTS and n-Octadecanethiol (98%, Sigma-Aldrich) were respectively utilized to hydrophobize the fluid cell and tipless cantilever for force measurements. Polished silicon wafers (prime class, N type, (1 0 0) orientation) were obtained from Lijing Technology Co., Ltd. Silica nanospheres (50 nm diameter) were procured from Shanghai Macklin Biochemical Technology Co., Ltd. PS powders with a molecular weight of ~35000 were sourced from Shanghai Aladdin Biochemical Technology Co., Ltd. Hydroxylated cellulose nanofibers (CNFs) were purchased from Tianjin Woodelf Biotechnology Co., Ltd. All the reagents and materials were used as received. Milli-Q water with a resistivity of 18.2 MΩ $cm^{-1}$ was supplied by an Ulupure-II-20 T water system.

All sample surfaces were prepared on silicon wafers. Prior to use, the wafers were ultrasonically cleaned in a water-ethanol mixture for 10 min, followed by drying with high-purity nitrogen. UV-Ozone treatment was then performed for 30 min to introduce hydroxyl groups and enhance surface reactivity. After UV treatment, the wafers exhibited a water contact angle of approximately 0°. AFM and SEM were employed to characterize the topography and root mean square (RMS) roughness of the resulting surfaces.

**Preparation of silicon-OTS surfaces.** Silicon-OTS surfaces were fabricated by exposing UV-activated silicon wafers to OTS vapor, with the surface hydrophobicity modulated by the treatment duration. Treatments of 30 min and 120 min resulted in water contact angles of ~45° and ~90°, respectively. After vapor deposition, the surfaces were rinsed sequentially with toluene, ethanol, and Milli-Q water to remove any residual OTS molecules.

**Preparation of crosslinked PDMS surfaces.** The Sylgard 184 PDMS precursor and curing agent were individually dissolved in hexane. The two solutions were then mixed at a mass ratio of 10:1 and ultrasonically degassed for 30 min. Thereafter, the mixture was deposited onto a hydroxylated silicon wafer and spin-coated at 5000 rpm for 30 s to ensure uniform spreading. The coated wafer was subsequently cured at 80 °C for 6 h. Finally, the sample surface was rinsed with toluene to remove any residual uncrosslinked oligomers, resulting in a crosslinked PDMS film.

**Preparation of brush PDMS surfaces.** Surfaces grafted with slippery PDMS brushes (brush PDMS) were fabricated following the grafting-from method[59]. First, silicon wafers were immersed in 10 mL of toluene (saturated with water) for 30 min. Prior to wafer immersion, toluene was mixed with DCDMS at a molar ratio of 20:1 and swirled for 30 s. The brush PDMS samples were then tilted to remove excess solution, followed by thorough rinsing with ethanol and Milli-Q water, and finally dried under a stream of nitrogen.

**Preparation of brush PDMS-NP surfaces.** Nanoparticles grafted with slippery PDMS brushes (brush PDMS-NP) were prepared using a method similar to that used for brush PDMS. UV-treated silica nanospheres (50 nm) were introduced into the above reactive solution at a concentration of 0.5 wt% and then sonicated for 30 min to ensure uniform dispersion. Silicon wafers were then immersed in the solution for 12 h to deposit PDMS-grafted silica nanoparticles onto the surface. The prepared brush PDMS-NP surfaces were thoroughly rinsed with toluene and Milli-Q water, and dried under a stream of nitrogen.

**Preparation of PS film.** PS solution was prepared by dissolving PS powders in toluene at a concentration of 0.5 wt%. PS films were prepared by spin-coating 1–2 drops of PS solution onto silicon

wafers at 5000 rpm for 30 s. The as-prepared PS films were subsequently placed under vacuum for 12 h to remove any residual solvent.

**Preparation of OTS-CNF surfaces.** PDAC and PSS were respectively dissolved at a concentration of 5 mg $mL^{-1}$ in a 0.5 M NaCl solution and assembled onto the surface using a layer-by-layer method[60]. Hydroxylated silicon wafers were sequentially immersed in PDAC and PSS solutions for 20 min, with rinsing in Milli-Q water following each immersion. After four cycles, a polyelectrolyte multilayer (PEM) was formed on the wafers. The PEM-coated surfaces were then capped with an additional PDAC layer. Subsequently, the PDAC-capped surfaces were immersed in a 1.0 mg $mL^{-1}$ solution of hydroxylated CNFs for 12 h, followed by rinsing with water and gentle drying under nitrogen. Finally, OTS was grafted onto the CNF-coated surfaces via chemical vapor deposition for 120 min to obtain OTS-CNF surfaces. After vapor deposition, the OTS-CNF surfaces were rinsed with toluene, ethanol and Milli-Q water to remove any residual OTS molecules.

**Preparation of OTS-NP surfaces.** UV-treated silica nanospheres (50 nm) were ultrasonically dispersed in ethanol at a concentration of 0.5 wt% for 30 min, after which hydroxylated silicon wafers were immersed in the solution for 12 h. OTS was then grafted onto the $SiO_2$-coated surface via chemical vapor deposition for 120 min. Finally, the OTS-NP surfaces were thoroughly rinsed with ethanol and Milli-Q water, followed by drying under a stream of nitrogen.

**Surface characterizations.** The morphologies of the fabricated surfaces were characterized by atomic force microscopy (AFM, Asylum Research MFP-3D-Bio) imaging operated in tapping mode under ambient conditions in air. The contact angles of as-prepared surfaces were measured using a contact angle goniometer (POWEREACH JC2000C1). The surface morphology of various samples was also characterized using a field-emission scanning electron microscope (FE-SEM, TESCAN MIRA5 LMH). Additionally, the morphology of tipless cantilever and attached bubble was examined using an inverted optical microscope (Olympus IX73).

## Force measurements

**AFM bubble probe and bubble manipulation.** Friction force measurements were performed using the bubble probe technique implemented on an MFP-3D-Bio atomic force microscope (AFM; Asylum Research, Santa Barbara, USA). A tipless rectangular cantilever (400 μm × 70 μm × 2 μm) featuring a circular gold patch was used to capture and manipulate a single bubble toward an adjacent substrate. The spring constant of cantilever was calibrated to be 0.3–0.4 N $m^{-1}$ using the Hutter-Bechhoefer method[61]. Prior to force measurements, AFM fluid cell was immersed in ethanol solution with 10 mM OTS for mild hydrophobization to temporarily immobilize bubbles. The cantilever was pre-hydrophobized in an ethanol solution containing 10 mM n-octadecanethiol for 24 h to facilitate stable bubble anchor.

Before friction measurements, bubble manipulation followed our reported AFM-based methodology[27,62]. Specifically, in Scheme I (Supplementary Fig. 18), an AFM cantilever was brought into proximity with a pre-existing bubble at the base of the liquid cell (i). The cantilever was then gently brought into contact with the bubble and retracted to lift it from the substrate, thereby forming a bubble probe (ii). To transfer the bubble to the measurement substrate, the target surface was positioned adjacent to the cantilever, establishing a transient three-phase configuration in which the bubble simultaneously contacted both interfaces (iii). The substrate was subsequently retracted in a controlled manner, inducing complete detachment of the bubble from the cantilever and its transfer onto the target surface (iv, v). Finally, the probe was driven to contact the upper surface of the bubble at zero deflection, enabling friction measurements (v, vi).

**Friction force measurement using Scheme I.** In a representative friction force measurement, bubbles with radii of 20–30 μm were generated at the bottom of water-filled AFM fluid cell by injecting gases of different components (e.g., air, $N_2$, $O_2$, $CO_2$) through an ultrasharp glass pipet. Following the bubble manipulation procedure described above, the bubble was transferred onto the vertically mounted test substrate for subsequent friction measurements. Before each friction measurement, the bubble-cantilever system was brought to mechanical equilibrium, and the cantilever deflection signal was adjusted to zero to incorporate the static buoyancy contribution into the baseline. The cantilever was then driven downward at a prescribed constant velocity (Supplementary Movie 9), mechanically pushing the attached bubble to slide along the substrate surface until a preset cantilever deflection was reached. During bubble sliding, the cantilever deflection was monitored in real time via a focused laser beam reflected from the cantilever surface towards a quadrant photodetector. Friction forces as a function of time were obtained by converting the monitored deflection based on Hooke's law using the AFM software (AR, version 16.33.234)[63]. Data analysis and plotting were performed using Origin 2024 (OriginLab). The estimated buoyancy force using Supplementary Eq. (5) was much smaller than the measured friction force (Supplementary Note 3). Friction experiments performed in the absence of bubbles yielded calibrated force signals near 0 nN (Supplementary Fig. 19) under identical driving conditions, confirming that the measured forces originated from bubble-surface friction rather than instrumental artifacts.

**Friction force measurement using Scheme II.** In another bubble friction measurement scheme, the bubble attached to the cantilever was transferred onto a substrate positioned beneath it. The substrate was then driven to move laterally (Supplementary Movie 10), with the expectation that the bubble would remain firmly anchored to the cantilever, thereby generating only relative motion at the bubble-substrate interface for friction measurement. During the measurement, the lateral deflection signal of the cantilever was monitored to characterize frictional resistance. However, once the substrate surface was hydrophobized, the bubble tended to adhere strongly to the surface, making it difficult to initiate relative movement between the bubble and hydrophobized substrate. Consequently, this method is applicable only to fully hydrophilic substrates, where a stable water film prevents the bubble from being highly pinned.

**Bubble motion verification.** Bubble motion during friction measurements was verified using inverted optical microscopy integrated with the AFM system. In Scheme I, the vertically mounted substrate allowed direct observation of the bubble from below (Supplementary Movie 9). In Scheme II, the horizontally mounted opaque substrate blocked the microscope view, and a CCD camera integrated with the AFM was used to monitor substrate motion from above (Supplementary Movie 10). To make substrate motion visually apparent, a defective substrate was used, and lateral translation was confirmed by tracking surface defects. No bubble rolling or spontaneous detachment was observed within the investigated velocity range (Supplementary Movie 11).

## Molecular dynamics (MD) simulations

In this study, molecular dynamics simulations were performed using the LAMMPS software package (version 2024) developed by Sandia National Laboratories[64–66]. The simulations visualized the discrepancy in the motion of various types of gas bubbles on surfaces with different OTS grafting coverages, which supports our research on bubble

friction. To deepen our understanding of the tribological behavior of gas bubbles in an aqueous environment, all-atom molecular dynamics simulations were further conducted to investigate the sliding of air, nitrogen, oxygen, and carbon dioxide bubbles on OTS grafted surfaces with high and low coverages.

Substrate modeling was performed using BIOVIA Materials Studio software (version 2023), and the silica (101) crystalline surface was selected as the substrate for grafting OTS molecules[67]. Firstly, hydroxylation reaction was simulated by introducing OH groups onto the terminal face. To prevent excessive packing and spatial effects arising from the steric effects of OTS molecules, which could compromise the structural rationality of the model, a spacing retention method was employed to remove certain OH groups. Supplementary Fig. 13 highlights the grafting vacancy sites with oxygen atoms designated by pink circles.

Secondly, the actual chemical reaction between OTS and silica is the condensation reaction between the Si-Cl bonds in the OTS molecule and the OH groups on the silica substrate, resulting in the formation of Si-O-Si bonds and the release of HCl. In the simulation, considering that a single OTS molecule has three Si-Cl groups, in order to simplify the grafting process, it is assumed that two of the Cl atoms are substituted by OH atoms and the third one is directly deleted by bonding with the substrate to form the Si-O-Si bond, as shown in Supplementary Fig. 14a. This method has been proven to be feasible and applied in numerous studies[68–70]. It should be noted that the hydrophobicity of silicon wafer, used as the bubble-sliding substrate in the experiments, was tuned by varying the exposure time to OTS vapor. To replicate this experimental condition during simulation, a Perl script was employed to randomly graft OTS molecules onto the silica substrate at varying grafting coverages, resulting in a more structured model. Owing to the inherent randomness of grafted OTS molecules, residual ungrafted oxygen atoms might persist on the substrate surface, necessitating secondary hydroxylation, as illustrated in Supplementary Fig. 14b. These residual uncovered regions are silanol groups rather than electronically active dangling-bond defects or unsaturated Si sites, thereby avoiding artificial chemisorption-active surface sites in the simulations[71].

The substrate model dimensions were set to 201.62 Å × 88.43 Å × 130 Å (X-Y-Z), as depicted in Supplementary Fig. 15a. The surfaces with high and low grafting coverages were shown in Supplementary Fig. 15b, c, respectively, with other modeling parameter remaining consistent. Due to the direct grafting of OTS molecules onto hydroxylated substrate by artificial design, unstable or localized high-energy configurations may occur. To ensure the adequate relaxation of surface structure, NVT systematic simulations of OTS-modified substrate/vacuum system were performed for 1 ns with a time step of 0.5 fs. The temperature was maintained to 300 K using a Nosé-Hoover thermostat, and the Newtonian equations of motion were solved by the Verlet algorithm.

Moreover, the configuration of gas molecules within the bubble in the simulated system is crucial. Numerous studies have demonstrated the ultra-high density of nanobubbles[72–75]. By combining theoretical calculations with high-resolution electrochemical measurements, the ultra-high density inside the bubble was revealed to be the key parameter for the stable existence of bubbles. Furthermore, it was found that the internal pressure and resultant density of the bubble increased with the decreased bubble volume, with internal pressures of 792, 647, and 518 atm for radii of 14, 18, and 22 Å, respectively. In addition, once a bubble attached to a surface, the internal gas density would increase, further leading to the enhancement of bubble stability. Based on the above findings, the radius and density of the bubble in this simulation were set to 15 Å and 0.6 g $cm^{-3}$, respectively. The molecular quantity inside the bubble was calculated based on the molar mass, and air was modeled as a mixture of gases with a mass ratio of oxygen to nitrogen (Supplementary Table 7).

The water molecules were modeled using the TIP3P water model, which accurately captured the structural and dynamic properties of water in MD simulations[76–78]. The water layer was generated with Packmol (version 20.15.1) and Moltemplate (version 2024) software, ensuring a total of 35,079 water molecules, corresponding to a density of no more than 33 molecules per cubic nanometer, thereby guaranteeing a reasonable molecular configuration. To prevent overlap between bubbles and water molecules and ensure appropriate spatial allocation, a region division command was employed to reserve adequate volume for bubbles. In addition, the SHAKE algorithm was applied to constrain the bond lengths and angles of water molecules, enhancing computational efficiency.

During the simulation, the Lennard-Jones (LJ) potential between water molecules, bubbles, and OTS-grafted surface was calculated by the following equations using the geometric mean mixing rule:

$$U_{\mathrm{LJ}}(r_{ij}) = 4\varepsilon_{ij}\left[\left(\frac{\sigma_{ij}}{r_{ij}}\right)^{12} - \left(\frac{\sigma_{ij}}{r_{ij}}\right)^{6}\right] \tag{1}$$

$$\sigma_{ij} = \frac{1}{2}(\sigma_{ii} + \sigma_{jj}) \tag{2}$$

$$\varepsilon_{ij} = \sqrt{\varepsilon_{ii}\varepsilon_{jj}} \tag{3}$$

where $r_{ij}$ is the distance between the centers of atoms $i$ and $j$, $\varepsilon_{ij}$ is the trap depth of the L-J potential that controls the strength of the short-range interaction, and $\sigma_{ij}$ denotes the L-J size parameter. The specific parameters of water and gas molecules are shown in Supplementary Table 8. The use of LJ-type intermolecular interactions corresponds to a physisorption framework dominated by non-bonded van der Waals interactions, which is appropriate for alkyl-terminated OTS surfaces and hydroxylated silica interfaces lacking chemically active adsorption sites[79].

Considering that bubbles slide along the surface following attachment, their geometric shape is closely related to the air contact angle at the three-phase interface. In the simulation, the bubble volume and geometry were defined based on experimental results, as shown in Supplementary Fig. 16. Notably, the air contact angle was dynamically adjusted during the subsequent relaxation process, based on the principles of system energy minimization and interaction force balance. This was intricately influenced by water-bubble and OTS-bubble interactions, as well as bubble solubility and deformation.

The cutoff radii for van der Waals and long-range electrostatic interactions were set to 8 Å and 10 Å, respectively. Long-range Coulomb interactions were computed using the particle-particle-particle-mesh (PPPM) method, with an accuracy threshold of $1 \times 10^{-4}$. The OTS molecules were modeled using the OPLS-AA force field, which has been shown to accurately predict tribological behaviors with a high degree of consistency with experimental results[80–82]. The classical all-atom MD with LJ-based non-bonded interactions provides an appropriate description for the present physisorption-dominated system[83]. The OPLS-AA potential function comprises four components: (1) the non-bonded interaction function between atoms; (2) the bond-stretching interaction function between atoms; (3) the bond angle bending interaction function; and (4) the dihedral angle torsion potential energy. The total potential energy is the sum of non-bonded and bonded interaction energies. The non-bonded interaction energy includes contributions from van der Waals forces and electrostatic interactions; while the bonded interaction energy encompasses bond stretching, bond angle bending, and dihedral torsion contributions.

The relevant equations are as follows:

$$E_{\text{total}} = E_{\text{bonded}} + E_{\text{non-bonded}} \tag{4}$$

$$E_{\text{bonded}} = E_{\text{bond}} + E_{\text{angle}} + E_{\text{dihedral}} \tag{5}$$

$$E_{\text{non-bonded}} = E_{\text{vanderWaals}} + E_{\text{electrostatic}} \tag{6}$$

$$E_{\text{bond}} = \sum_{\text{bonds}} K_r(r - r_0)^2 \tag{7}$$

where $K_r$ is the force constant, $r$ is the current bond length, and $r_0$ is the bond length equilibrium value.

$$E_{\text{angle}} = \sum_{\text{angles}} K_\theta(\theta - \theta_0)^2 \tag{8}$$

where $K_\theta$ is the force constant, $\theta$ is the current angle value, and $\theta_0$ is the angle value at equilibrium.

$$\begin{aligned} E_{\text{dihedral}} = \sum_{\text{dihedrals}} & \frac{K_0}{2} + \frac{K_1}{2}[1 + \cos(\phi)] + \frac{K_2}{2}[1 - \cos(2\phi)] \\ & + \frac{K_2}{2}[1 + \cos(3\phi)] + \frac{K_4}{2}[1 - \cos(4\phi)] \end{aligned} \tag{9}$$

where $K_O - K_4$ are force constants, and $\phi$ is the current value of the dihedral angle.

$$E_{\text{vanderWaals}} = 4\varepsilon_{ij}\left[\left(\frac{\sigma_{ij}}{r_{ij}}\right)^{12} - \left(\frac{\sigma_{ij}}{r_{ij}}\right)^{6}\right] \quad r < r_c \tag{10}$$

In this case, $\varepsilon_{ij}$ represents the depth of the potential, reflecting the strength of the attraction between two atoms. $\sigma_{ij}$ denotes the interatomic distance when the potential energy equals zero. The Lennard-Jones parameters for the interaction between distinct atom types $i$ and $j$ were calculated by geometrical rules:

$$\varepsilon_{ij} = \sqrt{\varepsilon_{ii} \cdot \varepsilon_{jj}} \tag{11}$$

$$\sigma_{ij} = \sqrt{\sigma_{ii} \cdot \sigma_{jj}} \tag{12}$$

$$E_{\text{electrostatic}} = \frac{Cq_iq_j}{\epsilon r} \quad r < r_c \tag{13}$$

Here, $C$ is the energy conversion parameter, $q_i$ and $q_j$ represent the charges of the two atoms, $\varepsilon$ is the dielectric constant of the medium, and $r$ is the distance between the two atoms. Based on the above equations, Supplementary Tables 9–12 summarize the relevant specific parameters for the OTS molecule.

As shown in Supplementary Fig. 16c, the simulation employed periodic boundary conditions in all directions, with a repulsive virtual wall applied along the Z-axis to control the movement of water and gas molecules, while maintaining the initial bubble pressure and restricting bubble expansion. Specifically, a repulsive 12–6 Lennard-Jones (LJ) virtual wall was placed at the upper $z$ boundary of the simulation box. In the LAMMPS input, this wall was implemented using fix wall/lj126 at ($z = 100$) Å, with $\epsilon = 1.0 \times 10^{-5}$ kcal mol $^{-1}$, $\sigma = 2$ Å, and a cutoff distance of 3 Å. The virtual wall only exerted a repulsive force in the normal direction when molecules approached the upper boundary and did not impose any tangential force along the bubble-sliding direction. Therefore, the lateral motion of the bubble was governed by the applied driving force and the gas-water-OTS interfacial interactions rather than by the virtual wall. To minimize computational demands, the substrate was fixed in place, allowing only the active silica layer to contact with OTS molecules. During the relaxation phase, the temperature was controlled using the Nose-Hoover thermostat, gradually increasing from 50 K to 300 K over 500 ps, and then maintained at 300 K for an additional 500 ps. The time step was set to 0.25 fs. In the subsequent bubble-slip simulation, a constant force was applied to gas molecules in the X-direction, with the temperature held at 300 K for 200 ps. The time step was set to 1 fs. For air (a mixture of gases) and carbon dioxide (composed of two elements), the acceleration of gas molecules within the bubble during sliding was set to be the same based on Newton's second law to prevent bubble rupture. The same constant force was applied to different-component bubbles to ensure the consistent initial force. The relevant forces were calculated and shown in Supplementary Table 13. Finally, the movement trajectory information was visualized and post-processed using OVITO software (version 3.10.4).

To quantify the residence behavior of gas molecules near the solid surface, a correspondence between atom IDs (first column) and molecule IDs (second column) was established from the *Atoms # full* section of the LAMMPS data file. Silicon-OTS-90, featuring more homogeneous OTS grafting, is selected as a representative model for this quantification. For each gas species, a small group of molecules initially located within the near-surface region was randomly selected and tracked throughout the simulation (Supplementary Table 5). These molecules were chosen to represent gas species that directly participate in interfacial processes occurring near the bubble-solid contact region. For each trajectory frame, all atoms belonging to the selected molecule IDs were extracted and used to calculate the molecular center-of-mass z-coordinate based on the atomic masses specified in the *Masses* section of the data file. The collective residence behavior of each gas species was evaluated using the group-averaged center-of-mass coordinate. Specifically, the mean $z$-coordinate of the selected molecules was calculated at every frame. The use of a group-averaged coordinate reduces the influence of short-time thermal fluctuations of individual molecules and provides a more robust measure of gas residence behavior at the interface. The reference position of the solid surface was defined as $z = 35.5$ Å. A near-surface contact region was then defined as $z = 35.5 \pm 3.0$ Å ($32.5 \le z \le 38.5$ Å). This interval approximately corresponds to the first interfacial molecular layer adjacent to the solid surface and was therefore used to identify gas molecules residing in direct proximity to the interface. When the group-averaged $z$-coordinate fell within this interval, the selected gas molecules were considered to reside within the near-surface region. Trajectory configurations were recorded every 0.1 ps. To minimize discretization errors arising from finite frame spacing, residence time was accumulated using linear interpolation between adjacent frames whenever the group-averaged coordinate crossed the boundaries of the predefined contact region.

## Statistics & reproducibility

No statistical method was used to predetermine sample size. No data were excluded from the analyses. The experiments were not randomized. The investigators were not blinded to allocation during experiments and outcome assessment.

## Reporting summary

Further information on research design is available in the Nature Portfolio Reporting Summary linked to this article.

## Data availability

The data supporting the findings of this study are available within the paper and its Supplementary Information. Source data are provided with this paper.

## Code availability

The code used in this study has been deposited in Figshare (https://doi.org/10.6084/m9.figshare.32605017) and is publicly available[84].

## References


1. Maeda, N., Chen, N., Tirrell, M. & Israelachvili, J. N. Adhesion and friction mechanisms of polymer-on-polymer surfaces. *Science* **297**, 379–382 (2002).
2. Shi, S., Wang, M., Poles, Y. & Fineberg, J. How frictional slip evolves. *Nat. Commun.* **14**, 8291 (2023).
3. Rapoport, L. et al. Hollow nanoparticles of $WS_2$ as potential solid-state lubricants. *Nature* **387**, 791–793 (1997).
4. Cumings, J. & Zettl, A. Low-friction nanoscale linear bearing realized from multiwall carbon nanotubes. *Science* **289**, 602–604 (2000).
5. Butt, H.-J., Berger, R., De Coninck, J. & Tadmor, R. Drop friction. *Nat. Rev. Phys.* **7**, 425–438 (2025).
6. McHale, G. et al. Adhesive Forces in Droplet Kinetic Friction on Liquidlike Surfaces. *Phys. Rev. Lett.* **135**, 204003 (2025).
7. Yan, X. et al. Bubble energy generator. *Sci. Adv.* **8**, eabo7698 (2022).
8. Zheng, H. et al. Electrically switched underwater capillary adhesion. *Nat. Commun.* **13**, 4584 (2022).
9. Guo, Z. et al. Efficient amino-acid-based reactive capture of CO2 via nickel molecular catalyst. *Nat. Commun.* **16**, 10373 (2025).
10. Prats Vergel, G. et al. Water dissociation efficiencies control the viability of reverse-bias bipolar membranes for CO2 electrolysis. *Nat. Chem. Eng.* **2**, 676–684 (2025).
11. Yuan, S. et al. Bubble evolution and transport in PEM water electrolysis: mechanism, impact, and management. *Prog. Energy Combust. Sci.* **96**, 101075 (2023).
12. Park, S. et al. Solutal marangoni effect determines bubble dynamics during electrocatalytic hydrogen evolution. *Nat. Chem.* **15**, 1532–1540 (2023).
13. Bikerman, J. J. Sliding of drops from surfaces of different roughnesses. *J. Colloid Sci.* **5**, 349–359 (1950).
14. Li, X. et al. Kinetic drop friction. *Nat. Commun.* **14**, 4571 (2023).
15. Sahli, R. et al. Evolution of real contact area under shear and the value of static friction of soft materials. *Proc. Natl. Acad. Sci.* **115**, 471–476 (2018).
16. Goyal, S. Planar sliding of a rigid body with dry friction: Limit surfaces and dynamics of motion. Cornell University: Ithaca, NY, 1989.
17. Stewart, D. E. Rigid-body dynamics with friction and impact. *Siam Rev.* **42**, 3–39 (2000).
18. Boltzmann, L. Further studies on the thermal equilibrium of gas molecules. in *The Kinetic Theory of Gases: an Anthology of Classic Papers with Historical Commentary* 262–349 (World Scientific, 2003).
19. Stephan, S. & Hasse, H. Molecular interactions at vapor-liquid interfaces: Binary mixtures of simple fluids. *Phys. Rev. E* **101**, 12802 (2020).
20. Liu, K., Vuckovac, M., Latikka, M., Huhtamäki, T. & Ras, R. H. A. Improving surface-wetting characterization. *Science* **363**, 1147–1148 (2019).
21. Kawasaki, K. Study of wettability of polymers by sliding of water drop. *J. Colloid Sci.* **15**, 402–407 (1960).
22. Karpitschka, S. et al. Droplets move over viscoelastic substrates by surfing a ridge. *Nat. Commun.* **6**, 7891 (2015).
23. Dimitrov, A. S., Kralchevsky, P. A., Nikolov, A. D., Noshi, H. & Matsumoto, M. Contact angle measurements with sessile drops and bubbles. *J. Colloid Interface Sci.* **145**, 279–282 (1991).
24. Drelich, J., Miller, J. D. & Good, R. J. The effect of drop (bubble) size on advancing and receding contact angles for heterogeneous and rough solid surfaces as observed with sessile-drop and captive-bubble techniques. *J. Colloid Interface Sci.* **179**, 37–50 (1996).
25. Daniel, D. et al. Origins of extreme liquid repellency on structured, flat, and lubricated hydrophobic surfaces. *Phys. Rev. Lett.* **120**, 244503 (2018).
26. Li, X. et al. *Salvinia*-like slippery surface with stable and mobile water/air contact line. *Natl. Sci. Rev.* **8**, 119–129 (2021).
27. Shi, C. et al. Measuring forces and spatiotemporal evolution of thin water films between an air bubble and solid surfaces of different hydrophobicity. *ACS Nano* **9**, 95–104 (2015).
28. Tabor, R. F., Chan, D. Y. C., Grieser, F. & Dagastine, R. R. Anomalous stability of carbon dioxide in pH-controlled bubble coalescence. *Angew. Chem. Int. Ed.* **50**, 3454–3456 (2011).
29. Del Castillo, L. A., Ohnishi, S., White, L. R., Carnie, S. L. & Horn, R. G. Effect of disjoining pressure on terminal velocity of a bubble sliding along an inclined wall. *J. Colloid Interface Sci.* **364**, 505–511 (2011).
30. Kibar, A., Ozbay, R., Sarshar, M. A., Kang, Y. T. & Choi, C.-H. Bubble movement on inclined hydrophobic surfaces. *Langmuir* **33**, 12016–12027 (2017).
31. Shi, C., Chan, D. Y. C., Liu, Q. & Zeng, H. Probing the hydrophobic interaction between air bubbles and partially hydrophobic surfaces using atomic force microscopy. *J. Phys. Chem. C.* **118**, 25000–25008 (2014).
32. Koh, X. Q., Thenarianto, C., Jokinen, V. & Daniel, D. Quantifying droplet–solid friction using an atomic force microscope. *Droplet* **3**, e107 (2024).
33. Yu, J. et al. Multivalent ions induce lateral structural inhomogeneities in polyelectrolyte brushes. *Sci. Adv.* **3**, eaao1497 (2017).
34. Chen, L., Huang, S., Ras, R. H. A. & Tian, X. Omniphobic liquid-like surfaces. *Nat. Rev. Chem.* **7**, 123–137 (2023).
35. Fakhraai, Z. & Forrest, J. A. Measuring the surface dynamics of glassy polymers. *Science* **319**, 600–604 (2008).
36. Feldmann, D. & Pinchasik, B.-E. How droplets move on surfaces with directional chemical heterogeneities. *J. Phys. Chem. Lett.* **12**, 11703–11709 (2021).
37. Lepikko, S. et al. Droplet slipperiness despite surface heterogeneity at molecular scale. *Nat. Chem.* **16**, 506–513 (2023).
38. Hauer, L. Phase separation in wetting ridges of sliding drops on soft and swollen surfaces. *Phys. Rev. Lett.* **130**, (2023).
39. Zhang, S. et al. Sticky yet slippery: Molecular ordering reconciles bubble-surface affinity with ultralow friction at the nanoscale. *Adv. Sci.* **e75495** (2026).
40. Brown, H. R. Chain pullout and mobility effects in friction and lubrication. *Science* **263**, 1411–1413 (1994).
41. Bootsma, A. N., Doney, A. C. & Wheeler, S. E. Predicting the strength of stacking interactions between heterocycles and aromatic amino acid side chains. *J. Am. Chem. Soc.* **141**, 11027–11035 (2019).
42. De Corato, M., Dimakopoulos, Y. & Tsamopoulos, J. The rising velocity of a slowly pulsating bubble in a shear-thinning fluid. *Phys. Fluids* **31**, (2019).
43. Gao, N. et al. How drops start sliding over solid surfaces. *Nat. Phys.* **14**, 191–196 (2018).
44. Khattak, H. K., Karpitschka, S., Snoeijer, J. H. & Dalnoki-Veress, K. Direct force measurement of microscopic droplets pulled along soft surfaces. *Nat. Commun.* **13**, 4436 (2022).
45. Zhao, B., Bonaccurso, E., Auernhammer, G. K. & Chen, L. Elasticity-to-capillarity transition in soft substrate deformation. *Nano Lett.* **21**, 10361–10367 (2021).

46. Pericet-Cámara, R., Best, A., Butt, H.-J. & Bonaccurso, E. Effect of capillary pressure and surface tension on the deformation of elastic surfaces by sessile liquid microdrops: an experimental investigation. *Langmuir* **24**, 10565–10568 (2008).
47. Zhang, L. Y., Lawrence, S., Xu, Z. & Masliyah, J. H. Studies of athabasca asphaltene langmuir films at air–water interface. *J. Colloid Interface Sci.* **264**, 128–140 (2003).
48. Wu, B. et al. Nanoparticle-stabilized oxygen microcapsules prepared by interfacial polymerization for enhanced oxygen delivery. *Angew. Chem. Int. Ed.* **60**, 9284–9289 (2021).
49. Qiao, C. et al. Recent advances in bubble-based technologies: Underlying interaction mechanisms and applications. *Appl. Phys. Rev.* **8**, 011315 (2021).
50. Ulman, A. Formation and structure of self-assembled monolayers. *Chem. Rev.* **96**, 1533–1554 (1996).
51. Love, J. C., Estroff, L. A., Kriebel, J. K., Nuzzo, R. G. & Whitesides, G. M. Self-assembled monolayers of thiolates on metals as a form of nanotechnology. *Chem. Rev.* **105**, 1103–1170 (2005).
52. Israelachvili, J. N. Intermolecular and Surface Forces. Academic Press: Waltham, MA, 2011.
53. Blake, T. D. The physics of moving wetting lines. *J. Colloid Interface Sci.* **299**, 1–13 (2006).
54. Qian, T., Wang, X.-P. & Sheng, P. A variational approach to moving contact line hydrodynamics. *J. Fluid Mech.* **564**, 333–360 (2006).
55. Dammer, S. M. & Lohse, D. Gas enrichment at liquid-wall interfaces. *Phys. Rev. Lett.* **96**, 206101 (2006).
56. *Polymer Adhesion, Friction, and Lubrication*. (Wiley, Hoboken, New Jersey, 2013).
57. Krasowska, M. & Malysa, K. Wetting films in attachment of the colliding bubble. *Adv. Colloid Interface Sci.* **134–135**, 138–150 (2007).
58. Parkinson, L., Sedev, R., Fornasiero, D. & Ralston, J. The terminal rise velocity of 10–100 μm diameter bubbles in water. *J. Colloid Interface Sci.* **322**, 168–172 (2008).
59. Liu, J. et al. One-step synthesis of a durable and liquid-repellent poly(dimethylsiloxane) coating. *Adv. Mater.* **33**, 2100237 (2021).
60. Huang, S. & Wang, D. A simple nanocellulose coating for self-cleaning upon water action: Molecular design of stable surface hydrophilicity. *Angew. Chem. Int. Ed.* **56**, 9053–9057 (2017).
61. Hutter, J. L. & Bechhoefer, J. Calibration of atomic-force microscope tips. *Rev. Sci. Instrum.* **64**, 1868–1873 (1993).
62. Xie, L. et al. Interaction mechanisms between air bubble and molybdenite surface: Impact of solution salinity and polymer adsorption. *Langmuir* **33**, 2353–2361 (2017).
63. Tabor, R. F., Manica, R., Chan, D. Y. C., Grieser, F. & Dagastine, R. R. Repulsive van der waals forces in soft matter: Why bubbles do not stick to walls. *Phys. Rev. Lett.* **106**, 064501 (2011).
64. Thompson, A. P. et al. LAMMPS-a flexible simulation tool for particle-based materials modeling at the atomic, meso, and continuum scales. *Comput. Phys. Commun.* **271**, 108171 (2022).
65. FrantzDale, B., Plimpton, S. J. & Shephard, M. S. Software components for parallel multiscale simulation: An example with LAMMPS. *Eng. Comput.* **26**, 205–211 (2010).
66. Plimpton, S. Fast parallel algorithms for short-range molecular dynamics. *J. Comput. Phys.* **117**, 1–19 (1995).
67. Meunier, M. & Robertson, S. *Materials studio* 20th anniversary. *Mol. Simul.* **47**, 537–539 (2021).
68. Barriga, J., Coto, B. & Fernandez, B. Molecular dynamics study of optimal packing structure of OTS self-assembled monolayers on $SiO_2$ surfaces. *Tribol. Int.* **40**, 960–966 (2007).
69. Roscioni, O. M., Muccioli, L., Mityashin, A., Cornil, J. & Zannoni, C. Structural characterization of alkylsilane and fluoroalkylsilane self-assembled monolayers on $SiO_2$ by molecular dynamics simulations. *J. Phys. Chem. C.* **120**, 14652–14662 (2016).
70. Yamamoto, H., Watanabe, T. & Ohdomari, I. A molecular simulation study of an organosilane self-assembled monolayer/$SiO_2$ substrate interface. *J. Chem. Phys.* **128**, (2008).
71. Zhuravlev, L. T. The surface chemistry of amorphous silica. *Zhuravlev model. Colloids Surf., A* **173**, 1–38 (2000).
72. Sun, Z., Gu, Z. & Ma, W. Confined electrochemical behaviors of single platinum nanoparticles revealing ultrahigh density of gas molecules inside a nanobubble. *Anal. Chem.* **95**, 3613–3620 (2023).
73. Gao, Z., Wu, W., Sun, W. & Wang, B. Understanding the stabilization of a bulk nanobubble: A molecular dynamics analysis. *Langmuir* **37**, 11281–11291 (2021).
74. Lei, J., Huang, D., Zhao, W., Liu, S. & Yue, Y. Investigating the stability mechanisms of single bulk nanobubbles: A molecular dynamics perspective. *Int. J. Heat. Mass Transf.* **225**, 125407 (2024).
75. Fang, H.-P. & Hu, J. Molecular dynamics simulation studies on some topics of water molecules on hydrophobic surfaces. *Nucl. Sci. Tech.* **17**, 71–77 (2006).
76. Mark, P. & Nilsson, L. Structure and dynamics of the TIP3P, SPC, and SPC/E water models at 298 K. *J. Phys. Chem. A* **105**, 9954–9960 (2001).
77. Price, D. J. & Brooks, C. L. III A modified TIP3P water potential for simulation with ewald summation. *J. Chem. Phys.* **121**, 10096–10103 (2004).
78. Kadaoluwa Pathirannahalage, S. P. et al. Systematic comparison of the structural and dynamic properties of commonly used water models for molecular dynamics simulations. *J. Chem. Inf. Model.* **61**, 4521–4536 (2021).
79. Hummer, G., Rasaiah, J. C. & Noworyta, J. P. Water conduction through the hydrophobic channel of a carbon nanotube. *Nature* **414**, 188–190 (2001).
80. Siu, S. W. I., Pluhackova, K. & Böckmann, R. A. Optimization of the OPLS-AA force field for long hydrocarbons. *J. Chem. Theory Comput.* **8**, 1459–1470 (2012).
81. Shahamat, M. & Rey, A. D. Equation of state modeling and force field-based molecular dynamics simulations of supercritical polyethylene+ hexane+ ethylene systems. *J. Mol. Graph. Model.* **100**, 107709 (2020).
82. Fang, C.-E., Tsai, Y.-C., Scheurer, C. & Chiu, C.-C. Revised atomic charges for OPLS force field model of poly (ethylene oxide): Benchmarks and applications in polymer electrolyte. *Polymers* **13**, 1131 (2021).
83. Weijs, J. H., Snoeijer, J. H. & Lohse, D. Formation of surface nanobubbles and the universality of their contact angles: a molecular dynamics approach. *Phys. Rev. Lett.* **108**, 104501 (2012).
84. Zhang, S. et al. Interfacial mechanisms of gas-bubble friction. figshare https://doi.org/10.6084/m9.figshare.32605017.v1 (2026).


## Author contributions

L.X. proposed the work. L.X. and H.Z. supervised the work. L.X. and S.Z. designed the experiments. S.Z. performed the force measurement experiments and analyzed the data under the supervision of L.X. H.T. prepared the solid surfaces, performed surface characterization, and assembled the data figures. S.Z. and H.T. produced the schematic illustrations. J.L. performed the molecular dynamics simulations. S.Z. wrote the manuscript. Z.L., J.W. and W.S. contributed to the discussion and interpretation of the results. L.X., H.Z. and H.-J.B. provided guidance on interfacial mechanisms, contributed to the interpretation of bubble friction, and revised the manuscript. All authors discussed the results, commented on the manuscript and approved the final version.

## Funding

This work was supported by the National Key R&D Program of China (2023YFC2908900), the Science and Technology Innovation Leading

Talent Program of Hunan Province (2024RC1018), the Natural Sciences and Engineering Research Council of Canada (NSERC), the Canada Foundation for Innovation (CFI), and the Canada Research Chairs Program.

## Competing interests
The authors declare no competing interests.

## Additional information
**Supplementary information** The online version contains supplementary material available at https://doi.org/10.1038/s41467-026-79472-y.

**Correspondence** and requests for materials should be addressed to Lei Xie or Hongbo Zeng.

**Peer review information** *Nature Communications* thanks Zuankai Wang, and the other, anonymous, reviewer(s) for their contribution to the peer review of this work. A peer review file is available.

**Reprints and permissions information** is available at http://www.nature.com/reprints

**Publisher's note** Springer Nature remains neutral with regard to jurisdictional claims in published maps and institutional affiliations.

**Open Access** This article is licensed under a Creative Commons Attribution-NonCommercial-NoDerivatives 4.0 International License, which permits any non-commercial use, sharing, distribution and reproduction in any medium or format, as long as you give appropriate credit to the original author(s) and the source, provide a link to the Creative Commons licence, and indicate if you modified the licensed material. You do not have permission under this licence to share adapted material derived from this article or parts of it. The images or other third party material in this article are included in the article's Creative Commons licence, unless indicated otherwise in a credit line to the material. If material is not included in the article's Creative Commons licence and your intended use is not permitted by statutory regulation or exceeds the permitted use, you will need to obtain permission directly from the copyright holder. To view a copy of this licence, visit http://creativecommons.org/licenses/by-nc-nd/4.0/.

© The Author(s) 2026

This Article in Press is shared early to give you faster access to new research. It is citable and carries a permanent DOI. The final edited version will replace it automatically.